Dynamic response of single crystalline copper subjected to quasi-isentropic, gas-gun driven loading

H. Jarmakani [a,*], J.M. McNaney [b], B. Kad [a], D. Orlikowski [b],
J.H. Nguyen [b], M.A. Meyers [a]

[a] *Materials Science Program, Mechanical and Aerospace Engineering Department, University of California,
San Diego, La Jolla, CA 92093 0418, United States*
[b] *Lawrence Livermore National Laboratory, Livermore, CA 94550, United States*

Abstract

A transmission electron microscopy study of quasi-isentropic gas-gun loading (peak pressures between 18 and 52 GPa) of [0 0 1] monocrystalline copper was carried out. The defect substructures at these different pressures were analyzed. Current experimental evidence suggests a deformation substructure that transitions from slip to twinning, where twinning occurs at the higher pressures (∼52 GPa), and heavily dislocated laths and dislocation cells take place at the intermediate and lower pressures. Evidence of stacking faults at the intermediate pressures was also found. Dislocation cell sizes decreased with increasing pressure and increased with distance away from the surface of impact. The results from the quasi-isentropic experiments are compared with those for flyer-plate and laser shock experiments reported in the literature. The Preston–Tonks–Wallace constitutive description is used to model both quasi-isentropic and shock compression experiments and predict the pressure at which the slip-twinning transition occurs in both cases. The model predicts a higher twinning transition pressure for isentropic than for shock experiments, and that twinning should not take place in the quasi-isentropic compression experiments given the loading paths investigated.
Published by Elsevier B.V.

Keywords: Isentropic compression; Twinning transition; Microstructural defects; Laser shock; Gas-gun; Copper

1. Introduction

The response of copper to very high strain-rate deformation is reasonably well understood. In particular, shock experiments on copper have been carried out for over 50 years. Techniques using explosives and flyer plates were first employed to create the compressive pulse in the material, and pressures attained were on the order of tens of GPa with accompanying strain rates on the order of 10^4 s^{-1} with durations on the order of microseconds or fractions thereof. Early experiments by Johari and Thomas [1] investigated defect substructures generated in explosively deformed copper and copper–aluminum alloys. More recently, laser pulses have been used to study shock compression in copper. The rapid heating and thermal expansion of the surface layers causes a shock to propagate through the material. Shock pressures higher than planar impact set-ups can be achieved (up to 75,000 GPa), and the strain rates attained are as high as

10^9 to 10^{11} s^{-1}. A basic difference is that the duration of the pulse in laser-shock is on the order of nanoseconds rather than microseconds.

In this work, however, quasi-isentropic compression experiments via gas-gun, are carried out on [0 0 1] copper, and the recovered deformation substructure is analyzed. The quasi-isentropic compression experiments (ICE) the quasi-isentropic compression experiments is a shockless process where very high pressure conditions can be accessed, and the accompanying temperature rise is much less severe than during shock experiments. The main motivation behind such a process is that the solid state of a material can be retained due to the lower temperatures experienced, and an understanding and characterization of the material response is, therefore, possible. In fact, quasi-isentropic experiments come very close to simulating conditions that occur in the depths of planets [2]. Entropy, the measure of the randomness of a system, does not change with depth in planets. Only temperature and pressure changes are experienced. ICE experiments in the early 1970s were aimed at mimicking these conditions.

* Corresponding author. Tel.: +1 858 534 6091; fax: +1 858 534 5698.
E-mail address: hjarmaka@ucsd.edu (H. Jarmakani).

Quasi-isentropic compression conditions can be achieved by various methods: gas-gun, laser, and magnetic loading. In our case, gas-gun loading is used. Early work on ICE with gas-gun by Lyzenga and Ahrens [3] used a composite flyer plate with materials of increasing shock impedance away from the target material. Barker [4] placed powders of varying densities along a powder blanket and pressed the blanket to produce a pillow impactor having a smooth shock impedance profile. Similarly, this current effort uses density graded impactors. In the case of ICE via laser, McNaney et al. [5] used a shockless laser drive setup to compress and recover an Al alloy. A smoothly rising pressure pulse is generated by focusing a laser beam on a reservoir material (carbon foam), creating a plasma that "stretches out" through a vacuum and discharges onto the sample. In magnetically driven experiments [6], the Z accelerator at Sandia National Labs (SNL) is capable of producing quasi-isentropic compression loading of solids using magnetic pulses. An advantage of this method is that a smoothly rising pressure profile can be generated without the initial spike at low pressures seen during impact experiments. Control over loading pressures and the rise time is also possible to meet experimental requirements [6].

2. Experimental procedure

2.1. ICE set-up

The two-stage gas-gun and experimental set up for this work are located at Lawrence Livermore National Labs (LLNL). Functionally graded material (FGM) impactors designed with increasing density profile (or shock impedance), as depicted in Fig. 1(a), were used to produce the smoothly rising pressure profiles [7]. Three different FGMs were used, each providing a certain density range. The first FGMs providing densities between 1.2 and 8 g/cm^3 consisted of aluminum and tungsten powders in a resin matrix. The second FGMs allowing for lower densities between 0.1 and 2.7 g/cm^3 incorporated a foam matrix, and the third allowing for a higher density range between 2.7 and
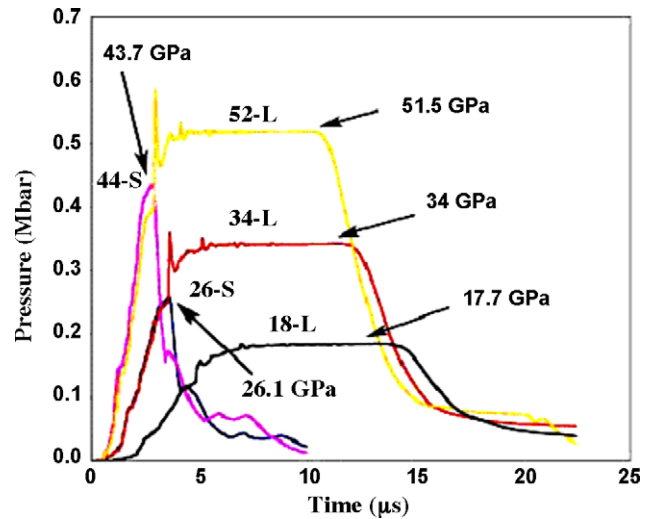
Fig. 2. Pressure profiles of ICE experiments.

15 g/cm^3 consisted of sintered aluminum and tungsten powders. The density is varied by simply adding these pre-mixed layers, each having a thickness of 200 ± 20 μm. The FGMs are usually made of 10–25 layers, allowing for the tailoring of specific thermodynamic paths during experimentation [9].

The copper samples were cylindrical, and their height and diameter were both 5 mm. The samples were press-fitted into a copper plate and lapped as one piece to ensure both sides were flat. The copper plate held seven samples that were simultaneously impacted during each experiment. A backing plate was placed on the back surface to transfer the shock and prevent reverberation. An illustration of the copper plate is presented in Fig. 1(b).

The pressure profiles in Fig. 2 were obtained from simulations (CALE, hydrodynamics code) carried out at LLNL that were benchmarked to data matched to experiments which had a velocimetry diagnostic. Five experiments, 52-L (1700 m/s), 34-L (1260 m/s), 18-L (730 m/s), 44-S (1760 m/s) and 26-S
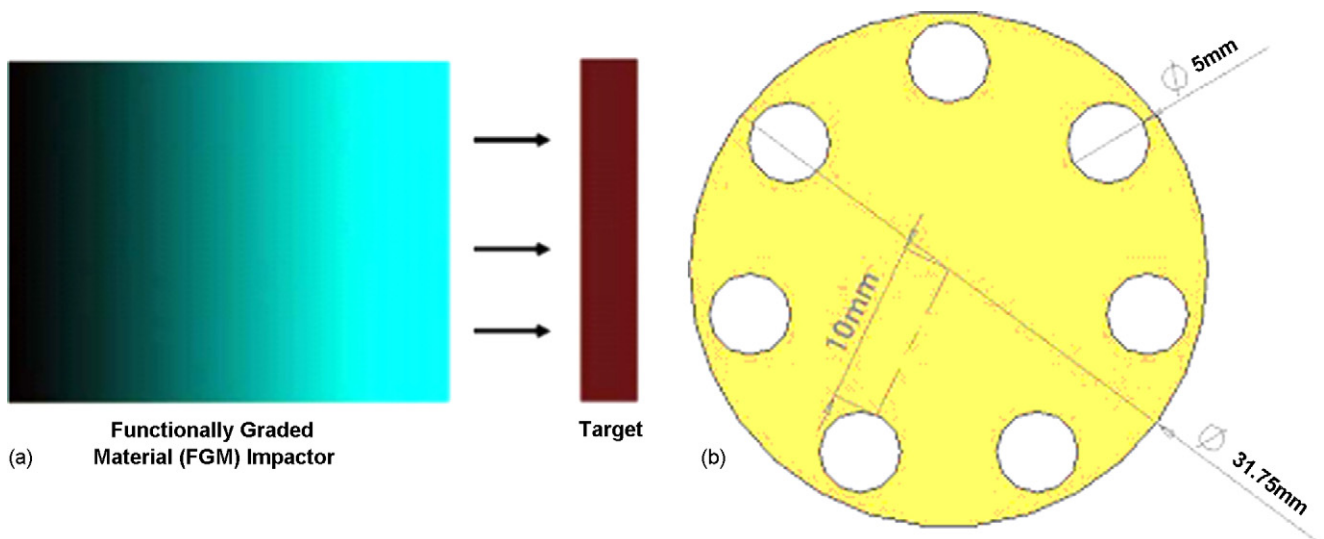
Fig. 1. (a) Illustration of FGM impactor hitting target (darkness proportional to density). (b) Illustration of copper plate into which the copper samples were press-fitted.

Table 1
Pressure profile data: strain, strain-rate, peak pressure

Set no.	Velocity (km/s)	Equivalent plastic strain (ε)	Strain rate ($\dot{\varepsilon}$ (s^{-1}))	Peak pressure (GPa)
A	1.7	−0.3	6.49×10^4	52
D	1.76	−0.23	5.67×10^4	44
B	1.26	−0.21	3.69×10^4	34
E	1.26	−0.15	4.44×10^4	26
C	0.73	−0.11	1.80×10^4	18

(1260 m/s), were carried out, with 52-L experiencing the highest pressure of 52 GPa and 18-L experiencing the lowest pressure of 18 GPa. Table 1 shows the pressures, strains and strain rates achieved in the different experiments. Two distinct pressure profiles were attained, one having a hold-time of approximately 10 μs ("long pulse"—L) and one having relatively no hold time (or a "short pulse"—S). The long-pulse samples belong to experiments 52-L, 34-L and 18-L, and the short-pulse samples belong to 44-S and 26-S. It should be noted that the "long-pulse" samples 52-L and 34-L exhibited a slight spike or shock at the onset of the pulse duration due to the experimental setup causing a deviation from the desired quasi-isentropic conditions. The likely effect on the microstructural deformation process is discussed in Section 3. In the case of experiments 44-S, 26-S and 18-L that were closest to the desired isentropic ideal, "shocking-up", which is the steepening of the isentropic wave into a shockwave as it propagates through the sample, did not occur in the CALE simulations. This was concluded by studying the temperature profiles generated by CALE, and a "jump" in temperature was not observed.

The as-recovered samples belonging to each batch were in the form of cylindrical specimens having an average diameter and thickness of 6 and 3.6 mm, respectively. Analysis of these samples enabled the comparison of the deformation mechanisms activated at this broad range of pressures. The strain rate versus pressure plot for these ICE experiments is given in Fig. 3. Strain rates achieved were on the order of $10^4 \, \text{s}^{-1}$. A comparison of the current data with shock experiments is provided in Section 4.
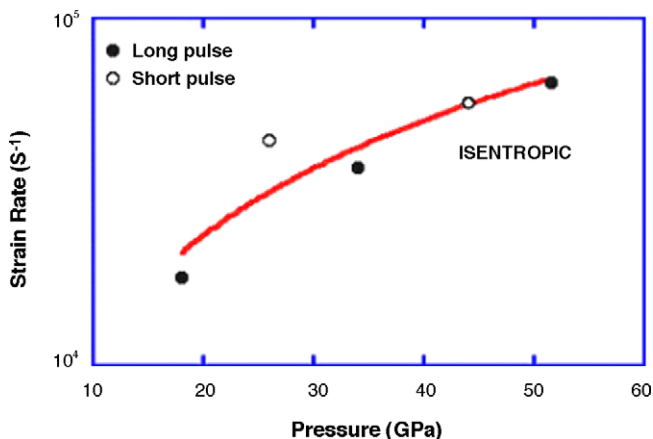

Fig. 3. Strain rate vs. pressure for ICE.

2.2. Micro-hardness measurements

Microhardness measurements were performed on all monocrystalline samples. After polishing to eliminate the heat affected zone (∼50 μm on each side) and provide a smooth surface, the impacted surface was indented using a Vickers tip attached to a Leco: M-400-H1 microhardness machine. Ten indents were taken on each polished surface, and the load applied was by a mass of 200 g, with a hold time of 15 s.

2.3. The transmission electron microscopy (TEM) sample preparation

Cylindrical cuts having a diameter of 3 mm were made through the center of each specimen by electrical discharge machining (EDM). Fig. 4 shows a typical as-recovered sample. TEM specimens were then sliced from each cylinder (as shown in Fig. 4). An average of four TEM foils was extracted from each sample. The specimens were further polished down using 1200, 2400, and 4000 grit paper, respectively, to about 100 μm. The foils were electropolished using a solution of 7% H_2SO_4 in methanol for TEM imaging.

3. Results and discussion

3.1. Microhardness results

An interesting trend in hardness was observed. The value increases with peak pressure until approximately 45 GPa, as illustrated in Fig. 5. It then saturates and begins to drop off dramatically. It can be seen that the hardness value at 52 GPa is almost two-thirds that of the intermediate pressure samples. It is hypothesized that the drop in hardness may be due to recovery processes taking place at the impact surface. This may be caused by the elevated temperature rise occurring at the higher peak-pressure conditions. Fig. 5 also shows this rise in temperature as the peak pressure increases.

3.2. TEM results

TEM results are presented next with an emphasis on the experiments closest to the intended quasi-isentropic ideal: 44-S, 26-S and 18-L. Although other deformation microstructures were observed, it should be noted that dislocation substructures such as cells and laths were most abundant in our TEM study. Twins and stacking faults were observed at the higher pressure experiments (52 and 44 GPa, respectively). These features can sometimes be indistinguishable without the use of high-resolution TEM. Our operative definition of twinning is strictly based on the formation of a twin diffraction pattern. If we do not see a twin diffraction pattern, but rather "fringes" in our images, then we conclude the defect is a stacking fault. Diffraction patterns taken from all samples investigated revealed a [0 0 1] crystal orientation, as seen in Fig. 6, confirming that sample orientation is not a variable in this study. This is to be expected as all impacted samples (from all five experiments) were cut out from the same [0 0 1] copper crystal.
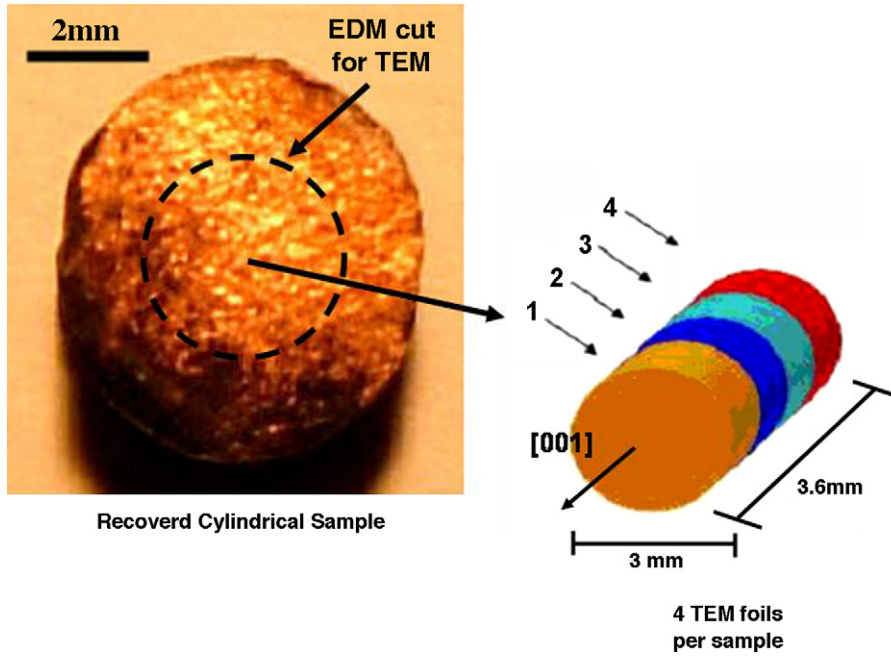
Fig. 4. As-recovered cylindrical sample showing EDM cut and schematic of the TEM foils extracted from recovered sample.
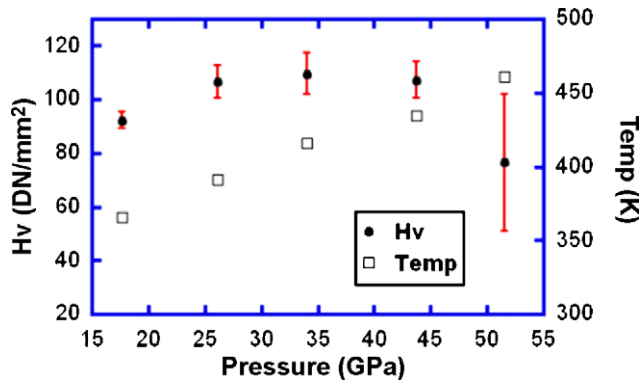

Fig. 5. Hardness and temperature vs. peak pressure.

3.2.1. Experiment 44-S

Dislocation cells were the predominant deformation substructure in the samples belonging to this group. Diffraction patterns with beam direction B = [0 0 1] confirmed the [0 0 1] crystal orientation of all samples investigated. At 0.15 mm (the closest distance from the impact surface investigated) within the specimen, dislocation cells with an average cell size of 0.36 μm, seen in Fig. 7(a), were evident. At approximately 2 mm (the farthest from the impact surface investigated) within the specimen, dislocation cells with an average cell size of 0.43 μm were evident. Table 2 summarizes the cell sizes measured at the various depths. Besides dislocation cells, elongated dislocation features (not as dense as those in 52-L) running along the $[\bar{2}\,\bar{2}\,0]$ direction
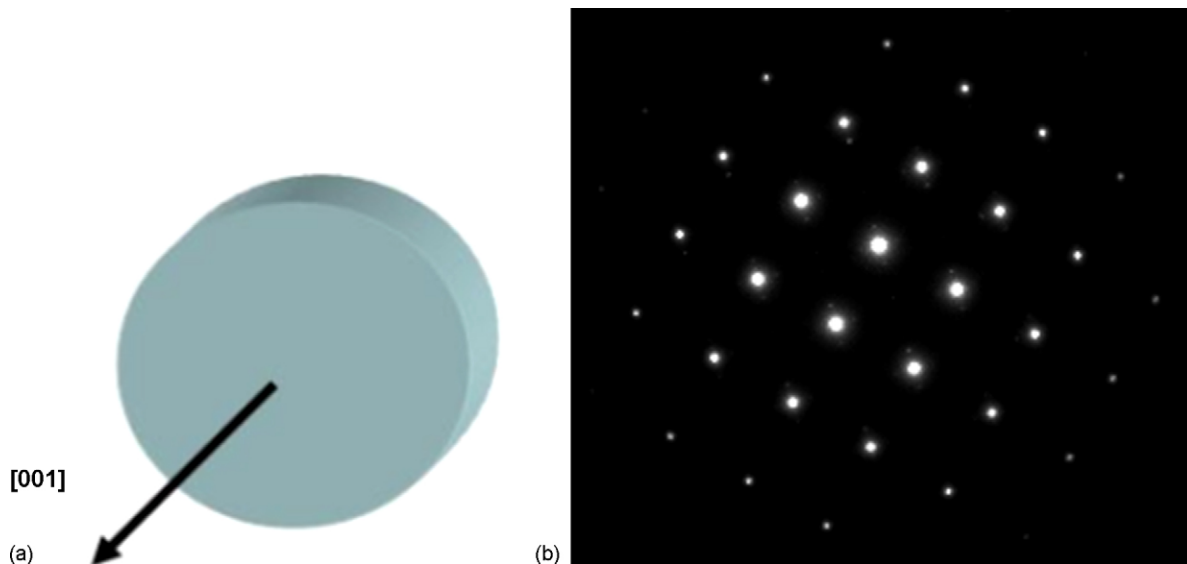

Fig. 6. (a) [0 0 1] orientation of all samples. (b) Typical diffraction pattern of samples indicating the [0 0 1] orientation.
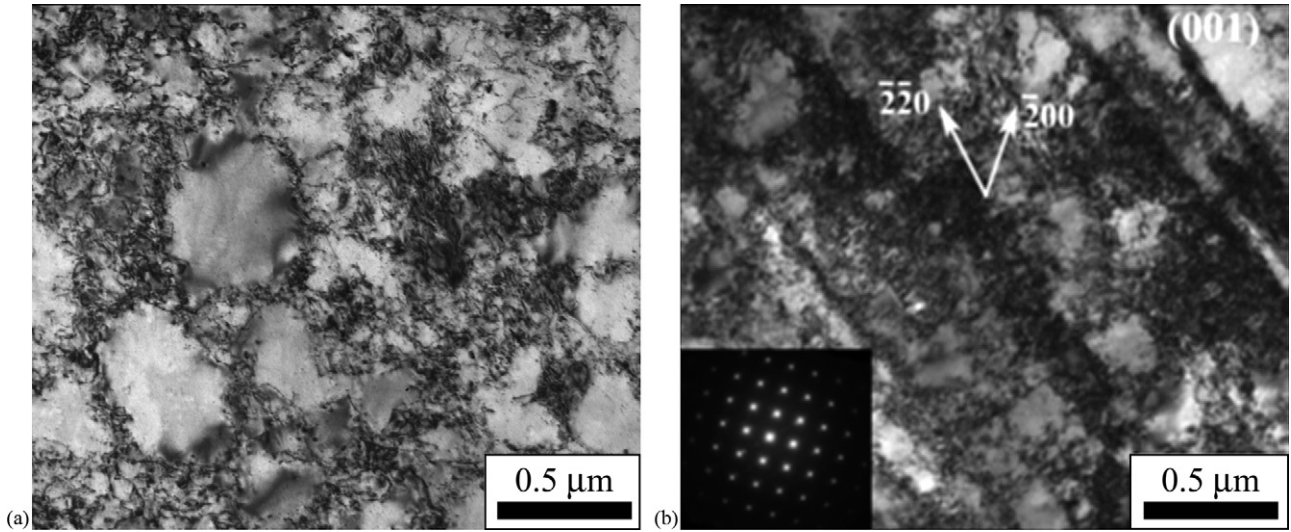
Fig. 7. (a) Sample 44-S, 0.15 mm deep—dislocation cells, average cell size: 0.36 μm; (b) dislocated laths and cells.

Table 2
44-S—features at various depths

Depth (mm)	Lath thickness (μm)	Lath spacing (μm)	Cell size (μm)
0.15	0.1	0.44	0.36
0.77	0.44	0.71	0.46
1.34	–	–	0.38
1.85	–	–	0.43

were present, Fig. 7(b). The features had a thickness of ∼0.1 μm with an average spacing between them of 0.44 μm.

At 0.77 mm from the impact surface, dislocation cells were predominant. Long dense laths/bands of dislocation walls were also observed, as seen in Fig. 8(a). Consistent with previous observations, the bands run along the [2 2 0] direction. The band thickness and spacing measured at this depth were 0.44 and 0.71 μm (summarized in Table 2). One interesting observation

comprised of two dislocated lath variants intersecting at a point, Fig. 8(b).

3.2.2. Experiment 26-S

Dislocation cells were the most abundant deformation features unveiled in this pressure condition. The average dislocation cell size increased from 0.4 μm at 0.25 mm within the sample to 0.5 μm at 2.7 mm (summarized in Table 3). Features such as stacking faults, dislocated laths and elongated cells were revealed in a few of the specimens explored, but they were not as abundant and occupied a much smaller area than the cells. At 0.9 mm from the surface, stacking faults were evident in a few isolated regions. Fig. 9(a) shows an example of such a region. The thickness of the stacking faults is about 80 nm, and the spacing between the bands is about 0.1 μm. One stacking fault variant stretches along the [$\bar{2}$ 2 0] direction. Further evidence of the same stacking fault variant was seen at 1.3 mm from the
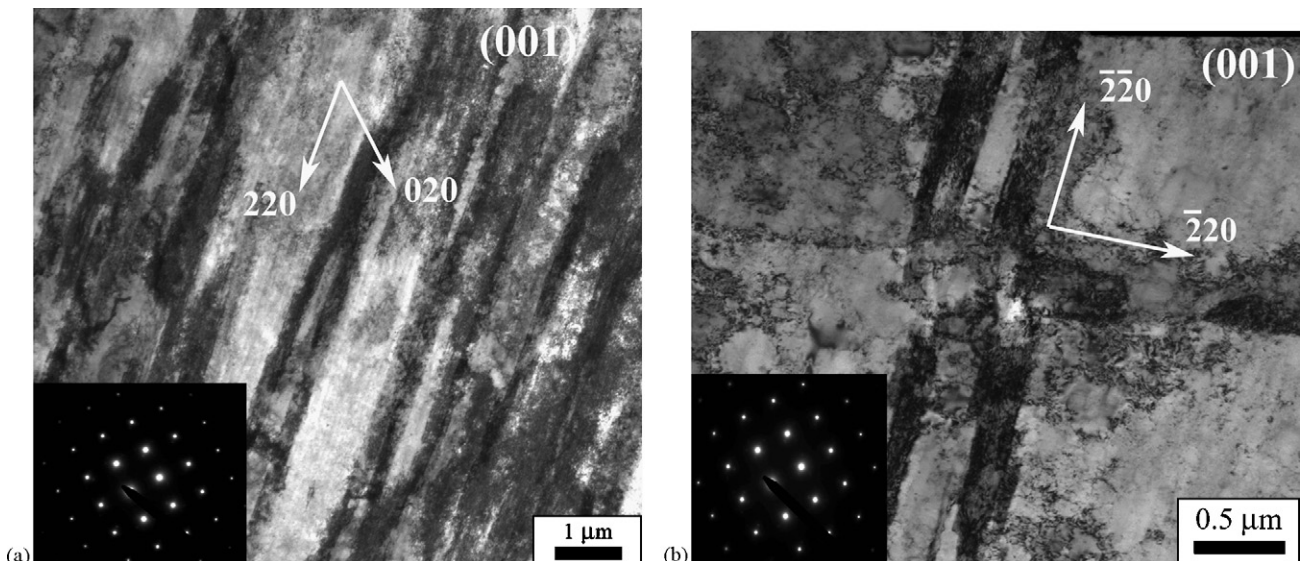

Fig. 8. Sample 44-S, 0.77 mm deep—(a) dislocated laths; (b) intersecting laths.
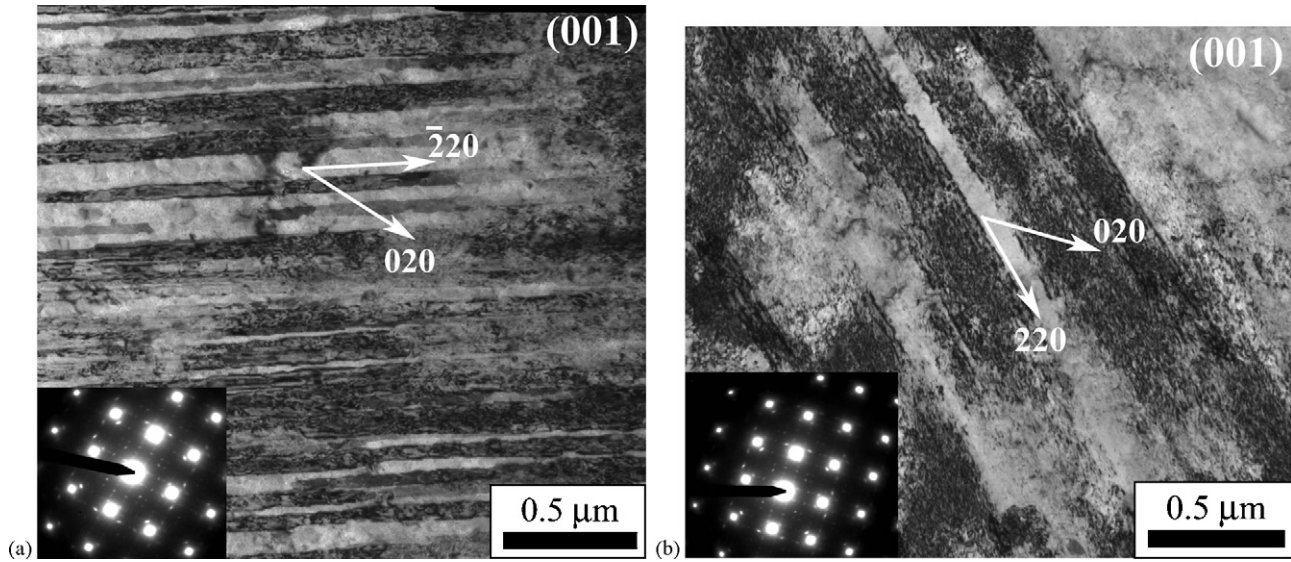
Fig. 9. (a) Sample 26-S, 0.9 mm deep—region of stacking faults along [$\bar{2}\,2\,0$]; (b) sample 26-S, 1.3 mm deep—stacking faults along [$2\,2\,0$].

Table 3
26-S—features at various depths

Depth (mm)	Stacking fault thickness (μm)	Stacking fault spacing (μm)	Cell size (μm)
0.25	–	–	0.4
0.9	0.08	0.1	0.42
1.3	0.3	0.13	0.4
1.8	0.28	1.21	0.49
2.7	0.291	0.73	0.5

impact surface, Fig. 9(b). The thickness of the features was larger ($\sim$0.3 μm), however, due to the pressure decay with distance. The average stacking-fault spacing was 0.13 μm.

At the same depth, narrow and heavily dislocated laths were observed, as seen in Fig. 10(a). The two lath variants perpendicular to each other can be seen running along the [$2\,2\,0$] and [$\bar{2}\,2\,0$]

directions, consistent with previous observations. An interesting area (not shown) within the sample at roughly 1.8 mm consisted of small slip-like features (along [$2\,2\,0$] direction) surrounded by a sea of dislocation cells. At 2.3 mm from the impact surface, dislocated laths and elongated dislocation cells, Fig. 10(b), were revealed. A summary of the thickness and spacing between the laths is provided in Table 3. The elongated cells are stretched along the same [$2\,2\,0$] orientation as that of the laths. This detail leads to the hypothesis that the laths at higher pressures closer to the impact surface relax into these elongated cells (and successively into regular dislocation cells) at lower pressures further away from the impact surface.

3.2.3. Experiment 18-L

Relatively large dislocation cells were the most abundant deformation feature for this lowest pressure condition. The aver-
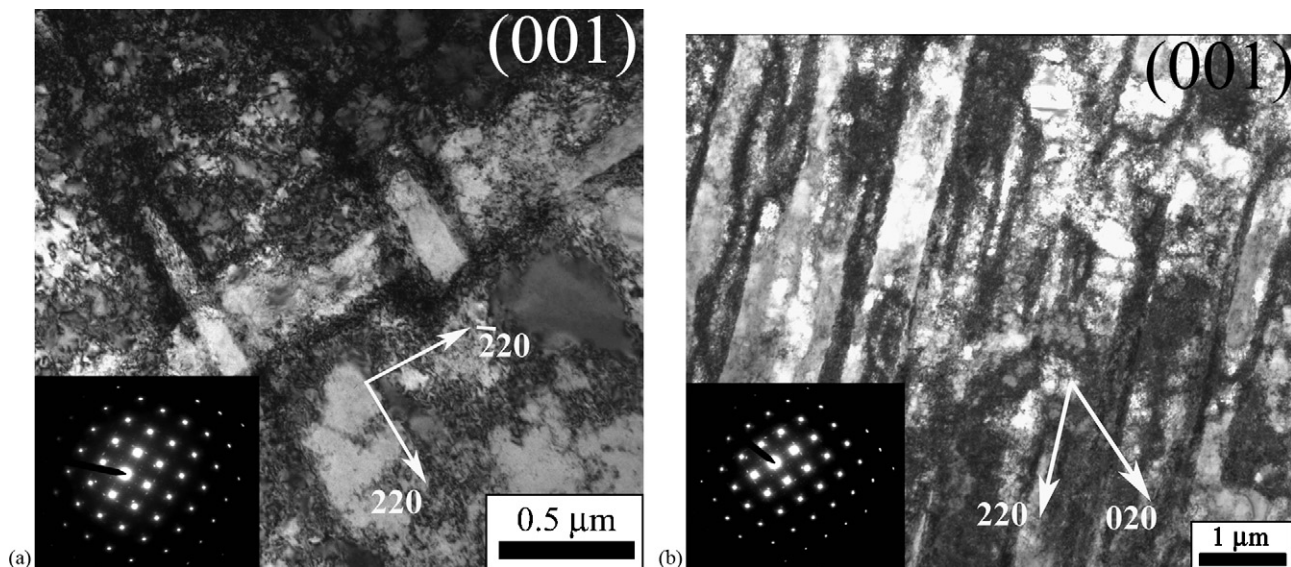

Fig. 10. (a) Sample 26-S, 1.3 mm deep—intersecting laths at 1.3 mm from impact surface; (b) 26-S, 2.3 mm—dislocated laths and some elongated cells.

Table 4
18-L—features at various depths

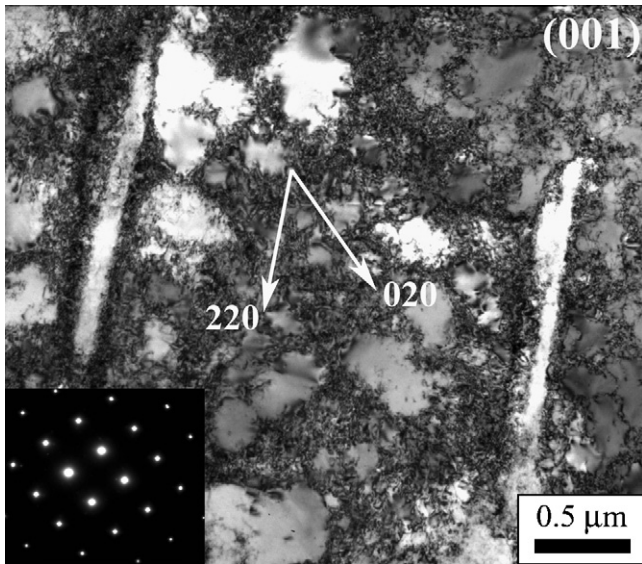| Depth (mm)	Cell size (μm)
0.13	0.44
0.15	0.55
0.67	0.62
0.72	0.64
1.3	0.41
1.9	0.63

Fig. 11. Sample 18-L, 0.13 mm—dislocation cells and laths/elongated cells.

age dislocation cell size varied from about 0.44 μm at 0.13 mm within the specimen to 0.6 μm at 2 mm. Table 4 provides a summary of the cell sizes with distance. Elongated cells and some lath-like activity were noticed in some regions, in particular closest to the impact surface at about 0.1 mm within the sample. Fig. 11 perfectly exemplifies the findings in this pressure group.

Both cells and dislocated lath-like features relaxing into elongated cells can be seen. The orientation of the laths/elongated cells is along the [2 2 0] direction. This orientation is the same as that of the laths observed in the previous experiments.

3.2.4. Experiment 52-L

TEM samples analyzed from 52-L revealed various deformation substructures. Dense dislocation substructures were most abundant. The size of dislocation cells close to the impact surface was too small to be discernable. At about 0.1 mm from the impact surface, the microstructure predominantly consisted of dislocation activity with some limited evidence of twining. The deformation features were rather inhomogeneous. Fig. 12(a) shows very clear twinned regions. The extra spots in the diffraction pattern confirmed the existence of these twins. At a beam direction B = [0 1 1], both small and large twins were observed having ($\bar{1}\,\bar{1}\,1$) twin habit planes. These micro-twins are embedded within dislocated laths running along the same direction as the twins (labeled in Fig. 12(a)). The smallest twins measured had a length of approximately 80 nm, and the longest twins were on the order of 1.5 μm. Longer twins existed in the TEM images, but they ran across the entire image and their full length was not captured. More TEM images at 0.1 mm from the surface taken with B = [0 0 1] showed stacking faults running along the [2 2 0] direction, Fig. 12(b). Their thickness and spacing are summarized in Table 5. In certain areas, dislocated laths were captured intersecting each other (not shown) at 90°.

Heavily dislocated laths were observed at 0.7 and 1.2 mm deep. Lath thickness and spacing are tabulated in Table 5. Fig. 13 shows laths 1.2 mm deep at a beam direction B = [0 0 1] running along the [2 2 0] direction. These features are in agreement with the "wavy sub-grains" observed after high-pressure shock compression of copper by Murr [8]. They are also analogous to the ones observed by Gray [9] in specimens where the residual strain was high. It is suggested that the substructures are due to thermal recovery of the microstructure. Additionally, twinning (not shown), confirmed by a diffraction pattern, was evident at this
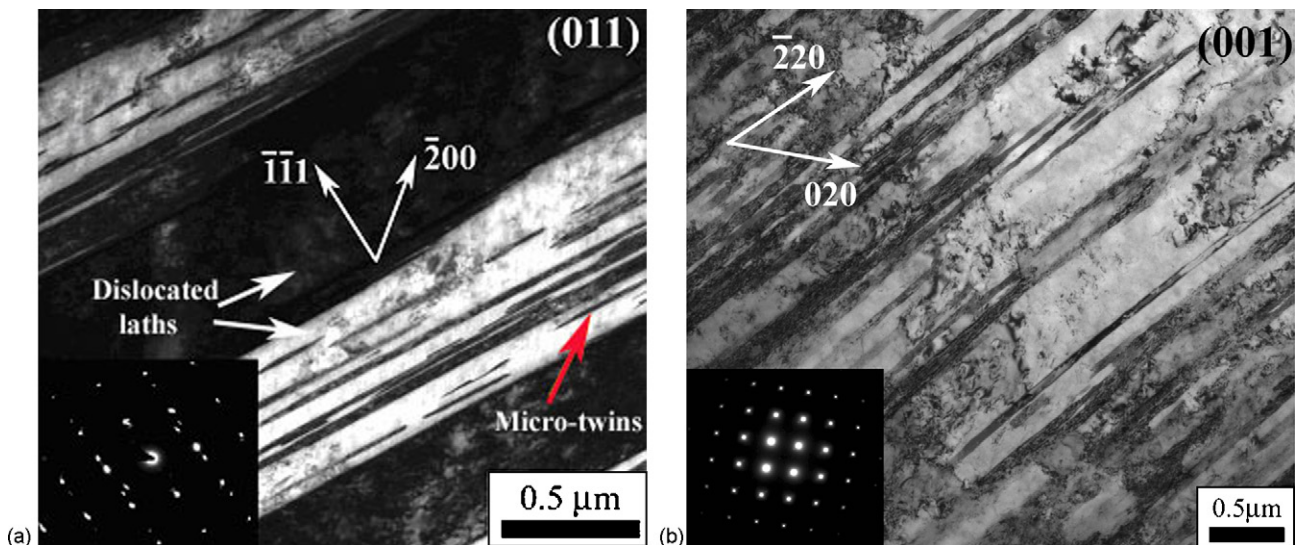

Fig. 12. Sample 52-L, 0.1 mm deep—(a) twinned regions showing dislocated laths and micro-twins, B = [0 1 1]; (b) stacking faults running along [$\bar{2}$ 2 0], B = [0 0 1].

Table 5
52-L—features at various depths

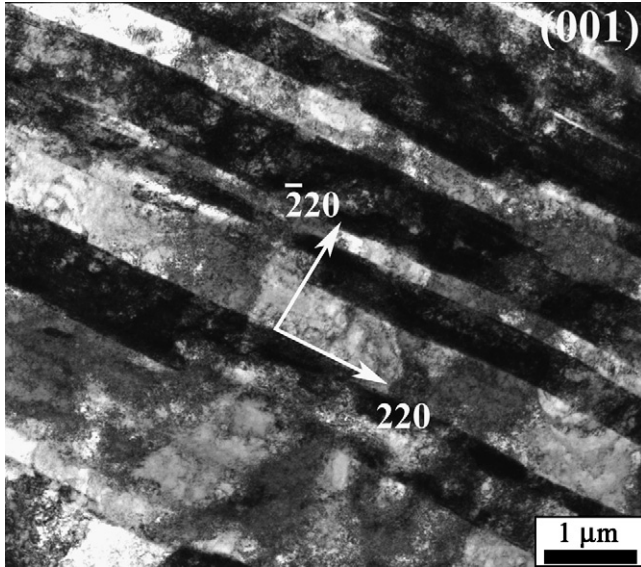| Depth (mm)	Twin thickness (μm)	Twin spacing (μm)	Twin length	Lath thickness (μm)	Lath spacing (μm)	Cell size (μm)	Stacking fault thickness (μm)	Stacking fault spacing (μm)
0.1	0.02	0.1	80 nm to 1.5 μm	0.48	0.45	–	0.053	0.13
0.7	–	–	–	0.6	0.45	–	–	–
1.2	–	–	–	0.7	0.4	0.15	–	–
1.8	–	–	–	–	–	0.2	–	–

Fig. 13. Sample 52-L, 1.2 mm deep, heavily dislocated laths running along [2 2 0].

depth. Dislocation cells were distinguishable at 1.2 mm deep (tabulated in Table 5).

3.2.5. Experiment 34-L

Dislocation cells were predominant at 0.14 mm from the impact surface of the specimens investigated in this group. The average cell sizes at the various depths investigated are tabulated

Table 6
34-L—features at various depths

Depth (mm)	Lath thickness (μm)	Lath spacing (μm)	Cell size (μm)
0.14	–	–	0.28
0.6	0.25	1.16	0.25
0.7	–	–	0.29
1	–	–	0.26
1.5	0.23	2.65	0.3

in Table 6. Dislocation bands were observed at 0.6 μm, seen in Fig. 14(a), running in the [2 2 0] direction. Two lath variants elongated in the [2 2 0] and [2 $\bar{2}$ 0] were also seen intersecting, Fig. 14(b). This is consistent with previous observations in 52-L and 44-S. The laths seem to act as either barriers to dislocation motion, thus, locking them in or as nucleation sites for dislocation activity. In addition to dislocation cells, heavily dislocated lath-like features were still evident at 0.7 and 1 mm running along [2 2 0]. Interesting features consisting of long laths/slip-like features with trapped in dislocations, identical to Fig. 14, were observed in a small region 1.5 mm deep (thickness and spacing tabulated). They were also stretched along the [2 2 0] direction.

3.3. Observations on cell-size

The plot shown in Fig. 15(a) summarizes the change in cell size with distance into the sample for the various pressure
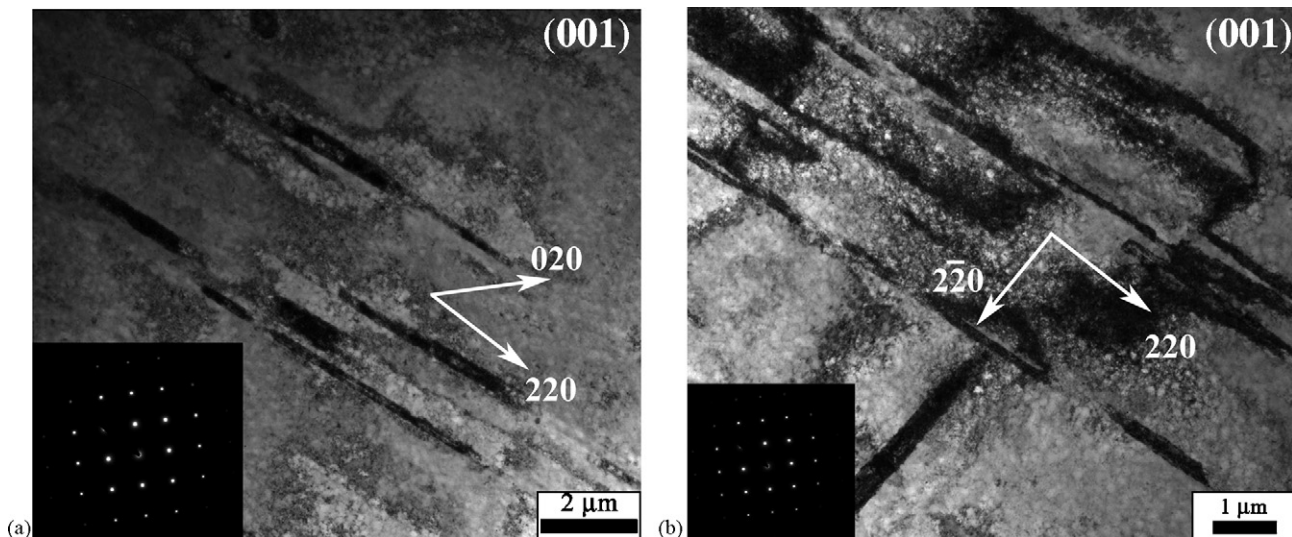

Fig. 14. Sample 34-L, 0.6 mm deep—(a) dislocated laths; (b) intersecting laths.
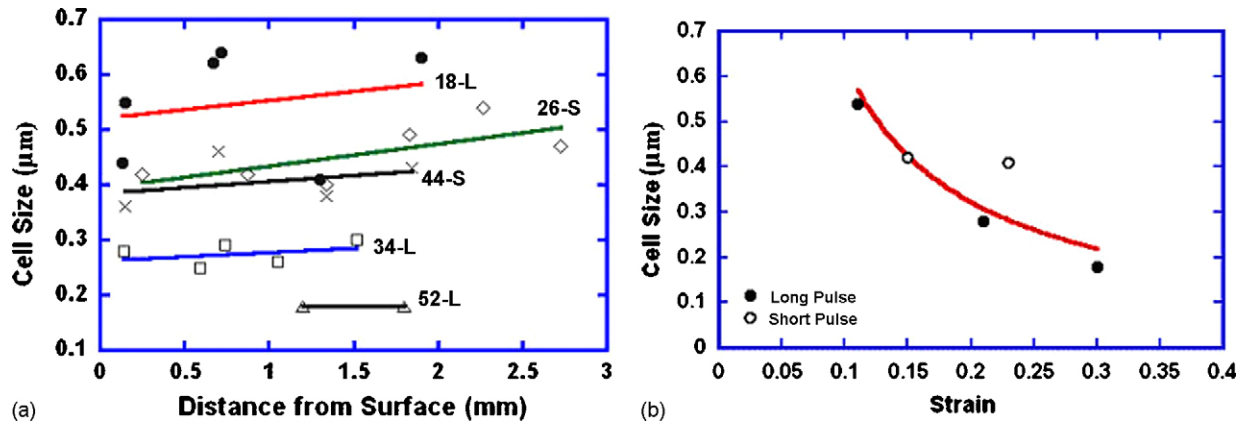
Fig. 15. (a) Cell size vs. distance from surface for all pressure conditions; (b) cell size vs. strain for all pressure conditions.

conditions considered. It can be seen that the cell size gradually increases with distance away from the impact surface for each pressure condition. This is consistent with previous investigations by [8–10]. In comparing the relative cell sizes of all the pressure conditions, two specifics that interfere with ideal experimental conditions need to be noted. First, experiments 52-L, 34-L and 18-L were subjected to a much longer pulse duration than that of 44-S and 26-S. The pulse duration was approximately 10 μs for 52-L, 34-L and 18-L as compared to less than 1 μs for 44-S and 26-S. Second, the CALE simulations reveal that 52-L and 34-L exhibit an unfavorable phenomenon; a slight shock at the onset of the pulse duration (due to the experimental setup). Experiments 44-S and 26-S are, therefore, much closer to the desired isentropic ideal that was intended.

The average cell size measured for 44-S is not consistent with measurements from the other experiments. Note that although 44-S experiences a higher peak pressure (44 GPa) than 34-L, it has larger cells. The cells in 44-S are also very close in size to those of 26-S, the other "short-pulse" experiment. Fig. 15(b) shows the change in cell size as a function of strain. The cell-sizes clearly decrease with increasing strain as is expected (with the exception of 44-S). Bassim and coworkers [11–14] have performed studies on the decrease in dislocation cell size with strain on copper and steel, and their work is consistent with our observations.

The "long-pulse" experiments, 52-L, 34-L, and 18-L, show a clear decrease in the average dislocation cell size with increasing peak pressure, consistent with prior work on high strain rate deformation of metals [8–10]. Sencer et al. [15] subjected copper samples to both a triangular and square-top shock wave to study the effect of pulse duration on the deformation microstructure (peak pressures were the same). They observed little variation in cell size in either case but noted that the dislocations were more irregular in shape in the triangle-top than in the square-top wave. In their work, Meyers and coworkers [8,16] note that dislocation cell structures are mostly dependent upon peak pressure and the time available to move these dislocations into arrays characterized by cell dimensions and wall size and structure. The dislocation cell size is, therefore, determined by the peak pressure whereas the wall structure and recognition of the cell structure are determined to a degree by the pulse duration which

relates to the available time for dislocations to reorganize into more stable energy configurations.

4. Comparison: ICE versus shock

A comparison of the recovered microstructure revealed in the quasi-isentropic compression experiments is made with that of shock compressed copper achieved via both explosively driven flyer plates and direct laser drives. The work of Cao et al. [17] on flyer-plate shock and Schneider et al. [10] on laser-shock of [0 0 1] copper is drawn upon. The peak pressures investigated in both cases are within the range of that studied in the ICE experiments (approximately 20–60 GPa) and are suitable for comparison purposes. In the case of flyer plate impact, an explosion drives a plate that impacts a target at a known velocity. The strain rates typically achieved and reported in literature are on the order of 10^6 s^{-1}, and pulse durations are on the order of 0.1–0.2 μs. This long pulse duration (also experienced in experiments 52-L, 34-L, and 18-L of the ICE experiments) allows shock generated defects to reorganize into lower energy configurations and allows more time for annealing and recrystallization to take place. Laser shock, on the other hand, is achieved by the rapid heating created by laser pulses illuminated on the material's surface. Strain rates reported in these experiments are on the order of 10^9 s^{-1}, and the pulse durations are on the order of 5 ns. Due to the very short pulse duration, the pressure decay in the sample is very rapid and post-shock heating is minimized.

Shock experiments are dictated by the following Swegle–Grady [18] expression:

$$\dot{\varepsilon}\,(\text{s}^{-1}) = 7.84 \times 10^{-33} P^4 \tag{1}$$

whereas the isentropic experiments have the following relationship derived from results of CALE simulations:

$$\dot{\varepsilon}\,(\text{s}^{-1}) = 1.17 \times 10^{-7} P^{1.1} \tag{2}$$

Fig. 16(a) compares the different strain rate regimes attained in shock and ICE. It is clear that strain rates achieved in shock are on the order of 10^9 s^{-1}, 10^4 to 10^5 orders of magnitude higher than ICE experiments. Fig. 16(b) shows the temperature rise in both cases. Clearly, the temperature rise is more severe in shock
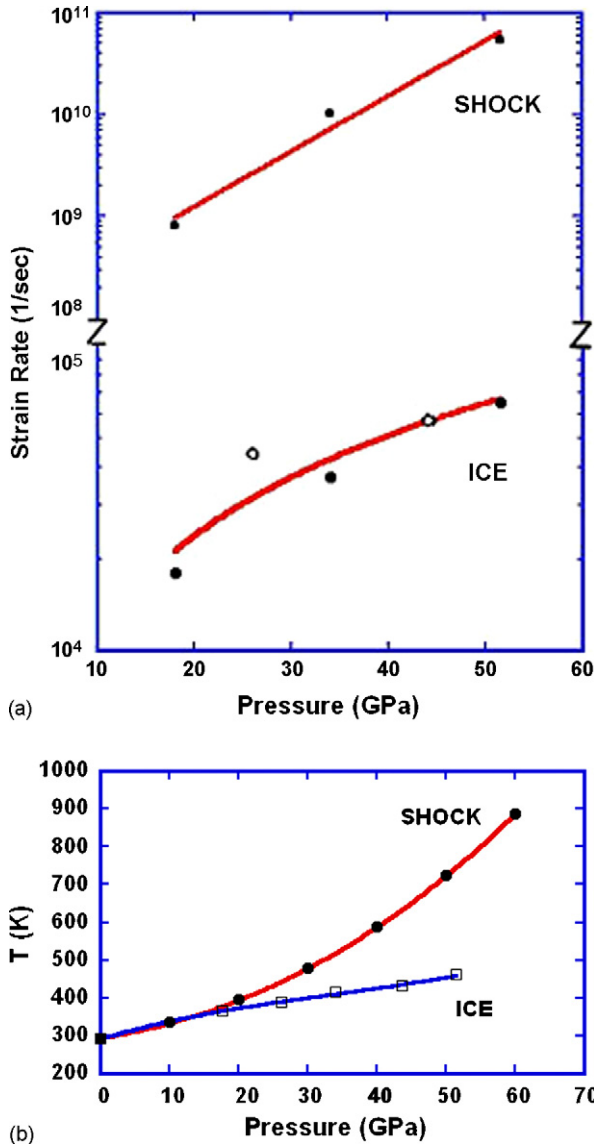
Fig. 16. (a) Comparison of the strain rate regimes attained in shock and ICE; (b) comparison of the temperature rise in shock and ICE.

at higher peak pressures as compared to ICE. The temperature rise for the ICE experiments was obtained from CALE simulation, and the rise for shock was calculated from thermodynamic relations and known equation of state parameters for copper.

4.1. Comparison of deformation substructures: 18–30 GPa

As discussed previously, dislocation activity was the main deformation behavior in the quasi-ICE experiments at 18 GPa. At 20 GPa, laser shock experiments exclusively contain well-defined cellular dislocations (not shown here) with an average cell size diameter between 0.2 and 0.3 μm [10]. This result is in accordance with previous investigations on shock by Murr [8]. The pulse duration was, however, 10–100 times higher in Murr's work. The plot in Fig. 17 shows that the dislocation cell-size in laser shock is significantly lower than in quasi-isentropic compression (0.25 μm versus 0.5 μm). This is attributed to the
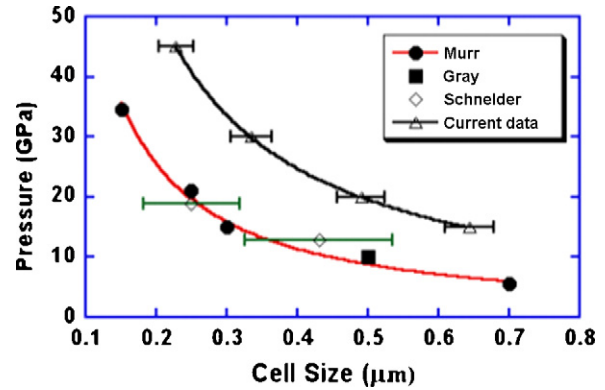

Fig. 17. Comparison of cell sizes at different pressures: ICE, laser-shock and flyer-plate impact.

much higher strain-rates achieved during laser-shock. The pulse duration is much longer in the ICE experiments, allowing for the defect substructures to relax and form a more stable energy configuration, and hence, larger dislocation cells. Some evidence of stacking faults (Fig. 9), as previously reported, was observed at 26 GPa in the ICE experiments. Stacking faults were seen at the higher pressure regimes in both flyer plate and laser shock (discussed next), but not between 18 and 30 GPa. In their work, Cao et al. [17] carry out experiments at 30 GPa and above. A comparison of the defect substructure for this pressure group with flyer-plate experiments is not made because of the lack of published data.

4.2. Comparison of deformation substructures: 30–40 GPa

Some similarity between all three cases was found in this range. In laser shock, this pressure regime produced dense dislocation tangles, stacking faults, and micro-twins. Fig. 18(a) shows stacking faults and dislocation tangles marked as DT and SF. There are no readily discernable dislocation cells, a clear indication of the pressure dependence of the deformation mechanisms. All four stacking fault variants *viz.* the partial dislocations $(1\,1\,\bar{1})1/6[1\,1\,2]$, $(1\,1\,1)1/6[\bar{1}\,\bar{1}\,2]$, $(\bar{1}\,1\,1)1/6[1\,\bar{1}\,2]$, and $(1\,\bar{1}\,1)1/6[\bar{1}\,1\,2]$ are observed. The stacking fault variants are along the same orientation in all three cases. Given the incident energy input as parallel to $[0\,0\,1]$, it is not surprising that all four stacking fault variants are activated in laser shock since they have the same critical resolved shear stress. The density of occurrence of the stacking faults along the $[\bar{2}\,2\,0]$ is, however, greater than along $[2\,2\,0]$ in laser shock. In ICE, the stacking faults and laths that are most abundant run along the $[2\,2\,0]$ direction. However, their occurrence is less frequent and not as abundant as in laser shock and flyer plate experiments. This is attributed to the difference in the strain rate regime in ICE (less by a factor of 10–100).

For the flyer plate experiments, stacking fault patterns similar to shock are observed at 30 GPa. Two sets of stacking faults along $[\bar{2}\,2\,0]$ and $[2\,2\,0]$ in the $(0\,0\,1)$ plane are shown in Fig. 18(b), where the TEM electron beam direction is $[0\,0\,1]$. These orientations are consistent with ICE experiments, since the same partial dislocations are active in both cases. The average spac-
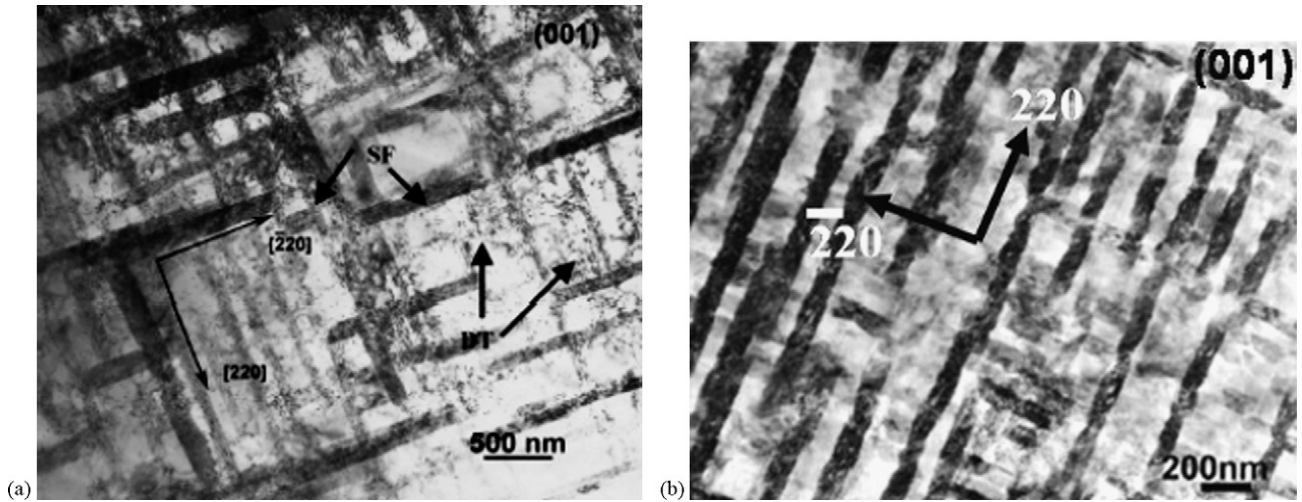
Fig. 18. (a) Stacking faults at 40 GPa in laser-shocked sample (from Schneider et al. [10]); (b) stacking faults at 30 GPa in flyer-plate impacted sample (from Cao et al. [17]).

ing between the stacking faults is between 230 and 450 nm for laser shock and between 180 and 220 nm for flyer-plate impact. The spacing in the ice experiments ranges between 100 and 500 nm.

4.3. Comparison of deformation substructures: 40–60 GPa

In laser shock, the deformation microstructure at 55 GPa consists of a high density of micro-twins (Fig. 19(a)) and laths (Fig. 19(b)). Two sets of micro-twins are observed when imaged at B = [0 0 1]. They appear at exactly 90° from one another aligned along [2 2 0] (set A) and [$\bar{2}$ 2 0] (set B) directions, respectively, and they are present roughly in same proportion (not shown here). When imaged in the edge orientation at B close to [$\bar{1}$ 0 1], Fig. 19(a), the micro-twins from set A have the (1 1 1) habit plane and are elongated along [1 $\bar{2}$ 1]. This set of micro-twins exhibits a wide range of lengths, from as small as 70 nm to as large as 1 μm. In contrast, the set B micro-twins have a near uniform length of 70 nm. Correspondingly, these two same

twin variants running along [2 2 0] [$\bar{2}$ 2 0] were also captured in the ICE experiments at 52 GPa.

Unlike the micro-twins, the laths in laser-shock are elongated close to ⟨2 2 0⟩. In some regions they are aligned along [$\bar{2}$ 2 0] and in others along [2 2 0]. Given the curvature of the laths it is unlikely that they conform to any single habit plane. The lath interface plane is parallel to [0 0 1] and therefore uniquely different from micro-twins. This microstructure represents the recovered state of a heavily twinned and dislocated structure. These laths are similar to those observed in the ICE experiments at 52 GPa, 0.7 and 1.2 mm from the impact surface. A striking similarity can be seen between the laths shown in Fig. 19(b) and those in Fig. 13. The laths are oriented along the [2 2 0] direction in both cases.

The flyer-plate samples shocked at 57 GPa revealed deformation bands, slip bands, recrystallized regions, dislocation tangles and some micro-twins. Only one set of micro-twins was observed having a ($\bar{1}$ $\bar{1}$ 1) habit plane, as seen in Fig. 20(a). The size of the micro-twins varies from 80 to 180 nm. Interestingly,
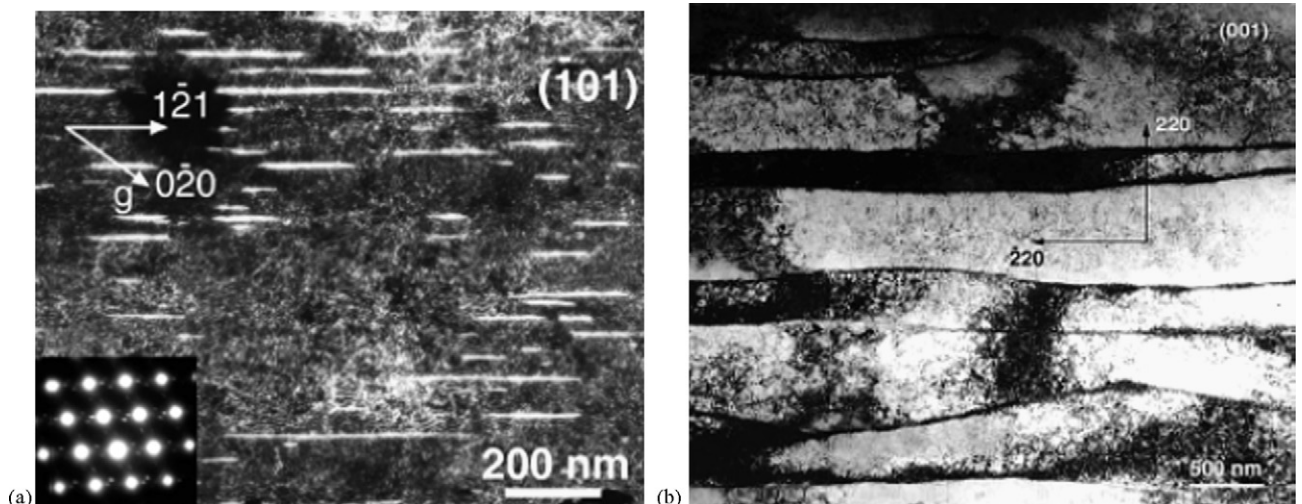

Fig. 19. (a) Micro-twins observed in laser shock at 55 GPa; (b) laths observed in laser shock at 55 GPa (from Schneider et al. [10]).
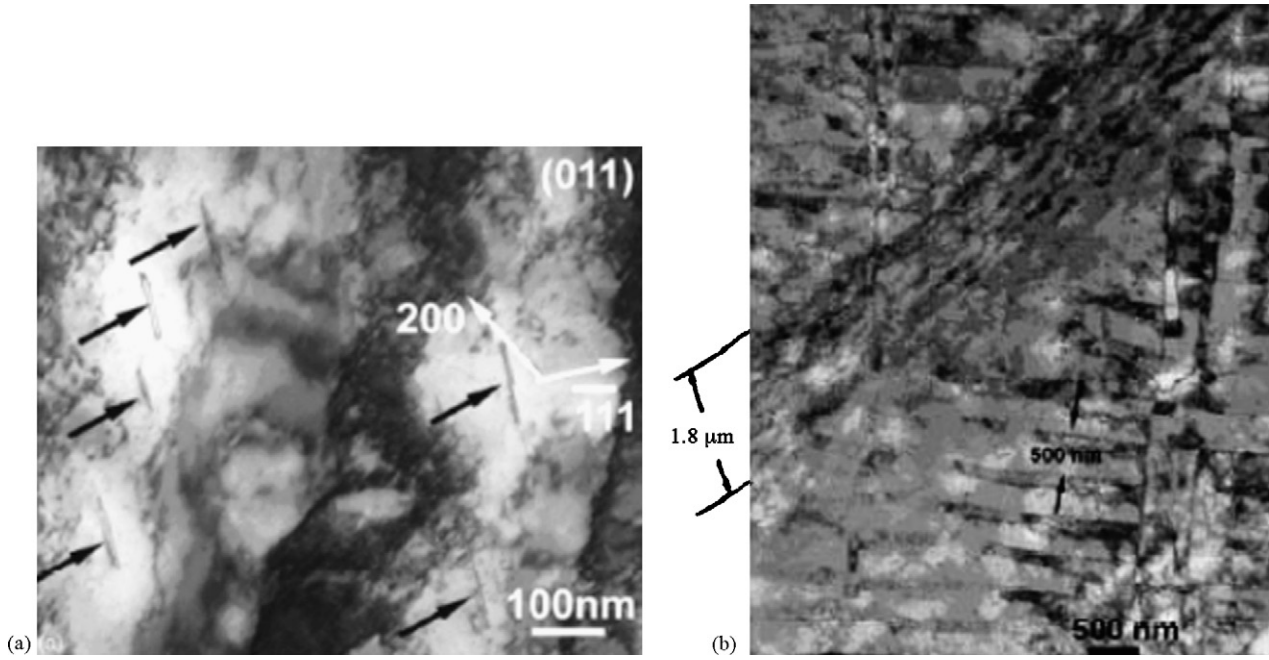
Fig. 20. (a) Micro-twins observed in plate impact at 57 GPa; (b) slip bands and stacking faults observed in plate impact at 57 GPa (from Cao et al. [17]).

the same micro-twin variant was observed in the ICE experiment at 52 GPa, elongated along the $[\bar{2}\,2\,0]$ direction. In one of the flyer-plate samples, a deformation band having a width of 1.8 μm is seen running diagonally along the sample, Fig. 20(b), intersecting smaller neighboring slip/stacking faults. Selected area diffraction identifies the vertical slip as $(1\,\bar{1}\,1)$.

The average width of the stacking faults observed was approximately 500 nm. Further into the sample, regular dislocation cell arrays running across the sample were observed (not shown here). Dislocation tangles between these arrays were also evident. The distance between the dislocation arrays were approximately 500 nm as well leading to the hypothesis that the arrays are due to the recovery or relaxation of the stacking-fault arrays. Similar to all three experiments, a decrease in dislocation density with depth into the sample is evident. Unlike the features seen in laser shock and ICE, fully recrystallized regions were seen in the flyer-plate experiments.

5. Constitutive modeling

The Preston–Tonks–Wallace constitutive equation is used to determine the critical pressure for twinning in both shock and ICE regimes. It is well-known that different metals have different threshold twinning pressures. In the case of FCC metals, this pressure is a function of stacking-fault energy [19]. Slip and twinning are visualized as competing mechanisms, where slip is a temperature and strain-rate dependent phenomenon and twinning is much less sensitive to these variables.

Using the general approach of Murr et al. [20] and Meyers et al. [21], we estimate the twinning threshold pressure for quasi-isentropic and shocked regions by considering the constitutive response of copper for the two regimes, shockless and shocked. The twinning threshold is taken to be the point at which the

tensile flow stress (e.g., 2τ) is equal to the tensile twinning stress, taken to be 490 MPa [21] in this work, and is assumed to be temperature and strain rate independent.

A number of models have been developed to estimate the flow stress as a function of strain rate and temperature [22,23] and additionally pressure [24–26]. With the exception of the Preston–Tonks–Wallace (PTW) constitutive description [24], none that allow for a pressure dependence are applicable over the range including both the thermal activation regime and the dislocation drag regime. Thus, in estimating the flow stress we will employ the model developed by PTW [24] as it is well suited for the very high strain rates in the experiments considered. If we restrict our analysis to constant strain rate paths, the instantaneous flow stress can be calculated from:

$$\tau = \hat{\tau}_s + \frac{1}{p}(s_0 - \hat{\tau}_y)\ln\left\{1 - \left[1 - \exp\left(-p\frac{\hat{\tau}_s - \hat{\tau}_y}{s_0 - \hat{\tau}_y}\right)\right]\right.$$
$$\left. \times \exp\left[\frac{-p\theta\psi}{(s_0 - \hat{\tau}_y)[\exp(p(\hat{\tau}_s - \hat{\tau}_y/s_0 - \hat{\tau}_y)) - 1]}\right]\right\} \quad (3)$$

where we have preserved the notation used in [24] for simplicity. The work hardening saturation stress and yield stress in the *thermal activation* regime are given by

$$\hat{\tau}_s = s_0 - (s_0 - s_\infty)\mathrm{erf}\left[\kappa\hat{T}\ln\left(\frac{\gamma\dot{\varepsilon}}{\dot{\psi}}\right)\right] \quad (4)$$

$$\hat{\tau}_y = y_0 - (y_0 - y_\infty)\mathrm{erf}\left[\kappa\hat{T}\ln\left(\frac{\gamma\dot{\varepsilon}}{\dot{\psi}}\right)\right] \quad (5)$$

where s_0, s_∞, y_0, and y_∞, are the values $\hat{\tau}_s$ and $\hat{\tau}_y$ take at zero and very high temperature, respectively, $\dot{\psi}$ the plastic strain rate, $\hat{T}$ the homologous temperature and erf is the error function. The flow stress is normalized to the shear modulus, G, e.g., $\hat{\tau}_y = \tau_y/G$. The parameters κ, γ are dimensionless material constants

and $\dot{\varepsilon}$ is given by

$$\dot{\varepsilon} = \frac{1}{2}\left(\frac{4\pi\rho}{3M}\right)^{1/3}\sqrt{\frac{G}{\rho}} \tag{6}$$

where M is the atomic mass and ρ is the density. The temperature dependence of the shear modulus was approximated as $G(\rho, T) = G_0(\rho)(1 - \alpha\hat{T})$, where $G_0(\rho)$ is the zero temperature modulus as a function of density and α is a material constant. The pressure dependence of the model is due to the pressure dependence of the shear modulus.

In the strong shock regime the behavior is given by

$$\hat{\tau}_s = s_0\left(\frac{\dot{\psi}}{\gamma\dot{\varepsilon}}\right)^{\beta} \tag{7}$$

$$\hat{\tau}_y = s_0\left(\frac{\dot{\psi}}{\gamma\dot{\varepsilon}}\right)^{\beta} \tag{8}$$

where β is a material constant and s_0 and γ are employed for continuity. In order to accommodate the observed increase in strain rate sensitivity at moderate strain rates an additional dependency is included as

$$\hat{\tau}_y = y_1\left(\frac{\dot{\psi}}{\gamma\dot{\varepsilon}}\right)^{y_2} \tag{9}$$

where y_1 and y_2 are the material constants.

The complete model is

$$\hat{\tau}_s = \max\left\{s_0 - (s_0 - s_\infty)\mathrm{erf}\left[\kappa\hat{T}\,\ln\left(\frac{\gamma\dot{\varepsilon}}{\dot{\psi}}\right)\right], s_0\left(\frac{\dot{\psi}}{\gamma\dot{\varepsilon}}\right)^{\beta}\right\} \tag{10}$$

$$\hat{\tau}_y = \max\left\{y_0 - (y_0 - y_\infty)\mathrm{erf}\left[\kappa\hat{T}\,\ln\left(\frac{\gamma\dot{\varepsilon}}{\dot{\psi}}\right)\right],\right.$$
$$\left. \times \min\left[y_1\left(\frac{\dot{\psi}}{\gamma\dot{\varepsilon}}\right)^{y_2}, s_0\left(\frac{\dot{\psi}}{\gamma\dot{\varepsilon}}\right)^{\beta}\right]\right\} \tag{11}$$

The model provides a smooth transition between the thermal activation regime and the strong shock regime.

In using the model to describe the $\langle 1\,0\,0\rangle$ single crystal used in this investigation the model parameters were slightly modified to match the low strain rate work hardening behavior for $\langle 1\,0\,0\rangle$ copper displayed in [19]. In particular the work hardening rate, θ, was adjusted to a value of 0.01 and saturation stress, s_0, to a value of 0.0045. All other parameters are as given in [24]. Although the flow behavior is a function of strain, strain rate, and temperature, at very high strain rates the flow stress is essentially at the saturation value for all values of strain. In the shockless region, the temperature, strain, and strain rate from the hydrodynamic solution previously presented were used. In the shocked region, the temperature and strain were taken from the simulations while the strain rates were determined as outlined above (Eq. (1)). It has also been assumed that the flow stress and twinning stress, being dependent on the atomic energy barrier, scale with the shear modulus, as is typical in high pressure constitutive models.
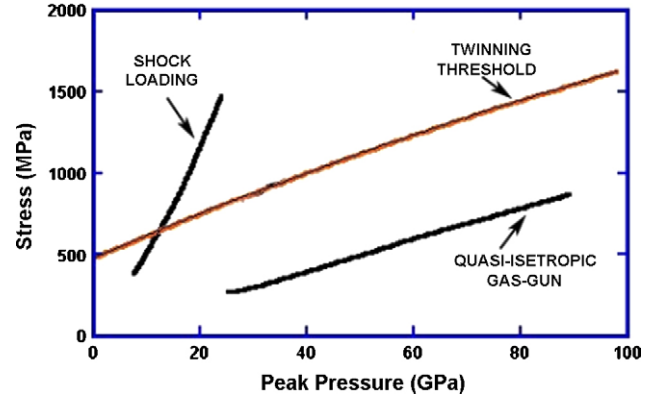

Fig. 21. Flow stress of [1 0 0] oriented copper vs. peak pressure in shock and ICE.

Results of these calculations are presented in Fig. 21 where the flow stress, as a function of peak drive pressure, for the shockless and shocked region are plotted. The twinning threshold was assumed to vary with pressure (or equivalently density) through the density dependence of G:

$$\sigma_T(P) = \sigma_T^0\frac{G(T, P)}{G_0} \tag{12}$$

where σ_T^0 and G_0 are the twinning threshold stress and shear modulus at ambient pressure, respectively. It can be seen from the figure that the slip-twinning transition in shock loading is approximately 18 GPa, in agreement with literature [2]. The steep shock loading curve arises due to the high strain-rate dependence on both the shock pressure and flow stress [7]. On the other hand, the isentropic gas-gun condition does not transition into the twinning regime and a critical twinning stress is, therefore, not reached. This is inconsistent with experimental observations, since twinning was observed at ~52 GPa. The presence of the shock at the start of the shock pulse (Fig. 2) for this pressure condition creates a deviation from quasi-isentropic conditions and may account for the presence of the observed twins.

6. Conclusions

- The deformation features seen in the quasi-isentropic compression experiments of monocrystalline copper are consistent with those seen in laser and flyer plate shock [1,2], but the pressures where the features dominate the response are quite different. For instance, the formation of stacking faults and twins occurs at lower pressures in shock as compared to ICE.
- The cell sizes in ICE are also uniformly larger than those left behind from shock (laser and flyer plate) even where the hold times are commensurate.
- The trend in cell size measurements obtained from the gas-gun ICE samples undergoing the long and short pulses reinforces previous observations that pulse duration may not be playing a key role in determining cell size.
- Our observations on cell size lead to the proposition that the loading path during ICE, through the lower strain rates and

temperatures attained, are having a real effect on the material response and causing production of fewer dislocations.

- The slight shock in experiments 52-L and 34-L caused a deviation from ideal quasi-isentropic conditions and may have been the reason there was a slight inconsistency in the peak pressure–cell size relationship.
- Experiments 44-S and 26-S that were closest to the quasi-isentropic ideal did not exhibit twins, but rather stacking faults, dislocated laths and cells.
- Modeling of the quasi-isentropic compression condition, using the Preston–Tonks–Wallace constitutive equation, revealed that twinning should not occur under the pressure regime investigated in these experiments.
- The presence of twinning in the experiments is attributed to the occurrence of an undesirable shock at the onset of the pulse duration due to the experimental set-up. This shock imparts larger strains and strain-rates, hence, causing twinning.

Acknowledgements

References

[1] O. Johari, G. Thomas, Acta Metall. 2 (1964) 113–1159.
[2] N. Holmes, Science and Technology Review, LLNL, Livermore, CA, 2000.
[3] G.A. Lyzenga, T.J. Ahrens, in: W.J. Nellis, L. Seaman, R.A. Graham (Eds.), American Institute of Physics Conference Proceedings No. 78, 1982, pp. 231–235.
[4] L.M. Barker, in: J.R. Asay, R.A. Graham, G.K. Straub (Eds.), Shock Waves in Condensed Matter, Elsevier Sci. Pub., Amsterdam, 1984.
[5] J.M. McNaney, M.J. Edwards, R. Becker, K.T. Lorenz, B.A. Remington, Met. Trans. A 35A (2004) 265.
[6] C.A. Hall, J.R. Asay, M.D. Knudson, W.A. Stygar, R.B. Spielman, T.D. Pointon, Rev. Scientific Instrum. 72 (2001) 3587.
[7] J.H. Nguyen, D. Orlikowski, F.H. Streitz, N.C. Holmes, J.A. Moriarty, in: M.D. Furnish, L.C. Chhabildas, R.S. Hixson (Eds.), AIP Conf. Proc., Melville, New York, 2004.
[8] L.E. Murr, in: M.A. Meyers, L.E. Murr (Eds.), Shock Waves and High-Strain Rate Phenomena in Metals, Plenum Press, New York, 1981, pp. 607–673.
[9] G.T. Gray III, in: M.A. Meyers, L.E. Murr, K.P. Staudhammer (Eds.), Shock Wave and High Strain Rate Phenomena in Materials, Marcel Dekker, New York, 1992, pp. 899–911.
[10] M.S. Schneider, B.K. Kad, D.H. Kalantar, B.A. Remington, M.A. Meyers, Metall. Trans. A 35 (2004) 263.
[11] M.N. Bassim, R.J. Klassen, Mater. Sci. Eng. 81 (1986) 163.
[12] M.N. Bassim, M.R. Bayoumi, Proceedings of the International Conference on Low-Energy Dislocation Structures, University of Virginia, August 10–13, 1986, pp. 317–324.
[13] M.N. Bassim, L.B. Huang, Mater. Sci. Eng. 96 (1988) 159.
[14] M.N. Bassim, R.J. Klassesn, Scr. Metall. 21 (1987) 625.
[15] B.H. Sencer, S.A. Maloy, G.T. Gray III, Acta Mater. 53 (2005) 3293–3303.
[16] M.A. Meyers, L.E. Murr, in: M.A. Meyers, L.E. Murr (Eds.), Shock Waves and High-Strain Rate Phenomena in Metals, Plenum Press, New York, 1981, pp. 487–530.
[17] B.Y. Cao, D.H. Lassila, M.S. Schneider, B.K. Kad, C.X. Huang, Y.B. Xu, D.H. Kalantar, B.A. Remington, M.A. Meyers, Mater. Sci. Eng. A 409 (2005) 270–281.
[18] J.W. Swegle, D.E. Grady, in: Y.M. Gupta (Ed.), shock Waves in Condensed Matter-1985, Plenum Press, New York, 1986, p. 353.
[19] M.A. Meyers, F. Gregori, B.K. Kad, M.S. Schneider, D.H. Kalantar, B.A. Remington, G. Ravichandran, T. Boehly, J.S. Wark, Acta Mater. 51 (2003) 12122.
[20] L.E. Murr, M.A. Meyers, C.-S. Niou, Y.-J. Chen, S. Pappu, C. Kennedy, Acta Mater. 45 (1997) 157.
[21] M.A. Meyers, O. Voehringer, V.A. Lubarda, Acta Mater. 49 (2001) 4025.
[22] F.J. Zerilli, R.W. Armstrong, J. Appl. Phys. 61 (1987) 1816.
[23] P.S. Follansbee, U.F. Kocks, Acta Metall. 36 (1988) 81.
[24] D.L. Preston, D.L. Tonks, D.C. Wallace, J. Appl. Phys. 93 (2003) 211.
[25] D.J. Steinberg, S.G. Cochran, M.W. Guinan, J. Appl. Phys. 51 (1980) 1496.
[26] D.J. Steinberg, C.M. Lund, J. Appl. Phys. 65 (1989) 1528.